ACS Photonics

pubs.acs.org/journal/apchd5 Article

Generation of Silver Metal Nanocluster Random Lasing

Chao-Chu Wang,[¶] Monika Kataria,[¶] Hung-I Lin,[¶] Amit Nain, Hsia Yu Lin, Christy Roshini Paul Inbaraj, Yu-Ming Liao, Anjali Thakran, Huan-Tsung Chang, Fan-Gang Tseng, Ya-Ping Hsieh, and Yang-Fang Chen*

Cite This: https://doi.org/10.1021/acsphotonics.1c01065 Read Online

ACCESS | Metrics & More | Article Recommendations | Supporting Information

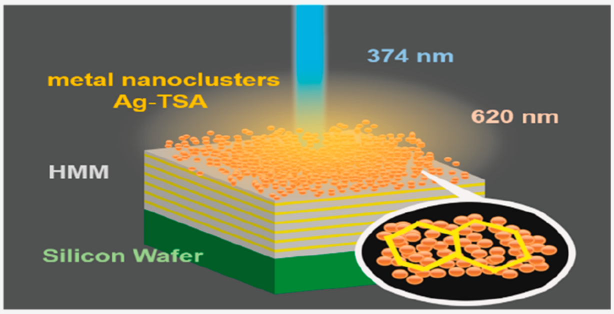

ABSTRACT: Atomically precise molecular-like metal nanoclusters (MNCs) exhibit unique properties, such as strong photoluminescence and absorption with inherent biocompatibility, which enable us to extend their applications to chemical sensing, biomedical imaging, optoelectronics, and many other areas. However, stimulated laser emission is greatly desirable to upgrade their more advanced functionalities. Here we provide a plausible approach to achieve this outstanding characteristic from MNCs. Quite interestingly, by integrating hyperbolic metamaterials (HMMs) with highly luminescent silver metal nanoclusters (Ag-TSA MNCs), a strong stimulated emission (random lasing action) with a low threshold of ∼0.5 kW cm^{-2} is discovered. The light emission is enhanced by ∼35 times when the solid-state assembly of Ag-TSA MNCs is integrated with HMM in comparison with that with a silicon substrate. The high-*k* modes excited by the HMM offer the possibility of forming the coherent closed feedback loops necessary for random lasing actions, thereby decreasing the energy loss associated with the photons' propagation in the matrix. The simulations derived from the finite-difference time-domain method support the experimental results. Our study shown here makes an initial step to demonstrate stimulated laser action from metal nanoclusters. It is believed that there exist many other alternatives for exploring this emerging research topic for the future development of cost-effective and biocompatible optoelectronic devices.

KEYWORDS: *metal nanoclusters, stimulated emission, random lasing, hyperbolic metamaterials, high-k modes*

INTRODUCTION

Researchers have been fascinated by noble-metal nanoparticles for decades owing to their applications in the fields of chemical sensing, optoelectronics, environmental science, and biomedical imaging.[1−7] The chemical, optical, and physical properties associated with metal nanoparticles greatly depend on their shape, size, and composition.[8−10] If the size of the metal nanostructures is >2 nm, then they can be categorized as plasmonics nanoparticles.[11] On the contrary, if the atomically precise molecular-like metal nanoparticles have a size of <2 nm due to strong quantum confinement effects at such small dimensions, then they exhibit discrete electronic states with semicontinuous electronic structures.[12] The so-called atomically precise molecular-like nanoparticles, termed metal nanoclusters (MNCs), have molecular-like properties such as molecular chirality, strong photoluminescence (PL), a HOMO−LUMO transition, and redox behavior.[13−16] The PL properties of MNCs have attracted the interest of researchers for their plausible distinctive usage in the fields of biomedical and optoelectronic applications and many other areas.[17] The well-known conventional semiconductor quantum dots have marked their presence in the previously mentioned applications but are limited by their stability and toxicity.[18,19] Here the highly stable luminescent MNCs enable us to overcome such existing limitations. Because there is an absence of heavy metals in the MNCs, they cease to possess toxicity and offer higher biocompatibility.[20] This unique feature makes the light emission properties of the MNCs pivotal to the research community and thus offers opportunities to work toward improving the light emission from the MNCs. In general, ligands are introduced into the metal core to prominently enhance the fluorescence intensity of MNCs approximately several ten-fold due to the interaction of the charges transfer on the shell of the metal clusters.[21] The performance of bright luminescence is intriguing for light−matter interactions, such as for chemo-sensors, bioimaging, novel probes, and drug screening. Recently, Deng et al. have successfully shown the fabrication of gold nanoclusters with a 65% PL quantum yield for green emissions via host−guest

Received: July 15, 2021

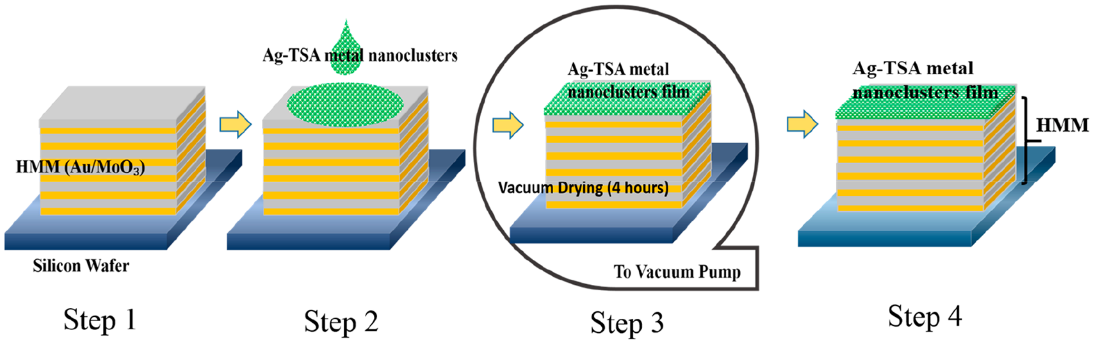

Figure 1. Schematic diagram of the fabrication process followed in fabricating the lasing device composed of silver metal nanoclusters (Ag-TSA MNCs) and hyperbolic metamaterials (HMMs).

recognition.[22] Soldan et al. reported that the gold doping of silver nanoclusters resulted in a 26-fold enhancement in the luminescence quantum yield.[23] However, the literature on MNCs is limited to spontaneous emissions. Research beyond the conventional thinking is required to further explore the possibility of stimulated emissions from MNCs,.

The use of hyperbolic metamaterials (HMMs) of multilayers of metals and dielectric materials to create devices with subwavelength-small dimensions is one of the excellent alternatives for achieving stimulated emission arising from MNCs.[24] HMM is highly efficient at absorbing and confining light with a number of fundamentally unusual properties.[25] The dielectric constant as a function of frequency shows the field inside the material change in response to the electromagnetic wave passing through it and is used to characterize the optical wave propagation in the material.[26] The dispersion relation represents the allowed propagation directions and their corresponding wavelengths. Moreover, the photonic density of states (PDOS) increases because the unique hyperbolic unlimited wave vectors (i.e., high-*k* modes) of the iso-frequency contour in the momentum space.[26−31] Once the metal and the dielectric interface is thin and flat, a collective oscillation of electrons called surface plasmon polaritons (SPPs) is confined to the interface. In addition, the high-*k* modes that emerge from the intercoupling effect of SPPs are realized as the volume plasmon polaritons, resulting in an enhancement of charge-transfer dynamics, an improvement in fluorescence emission, incremented transition rates of optical gain media, and a higher possibility of achieving laser action.[26,32]

In this work, we make an attempt to demonstrate HMM-assisted random lasing emissions from the solid-state assembly of silver metal nanoclusters (Ag-TSA MNCs). Compared with conventional lasers, random lasers possess several advantages, including being angle-free, cost-effective, biocompatible, and so on, which are very useful, spanning from bioimaging to solid-state lighting.[33−37] In particular, a recent demonstration of an electrically driven quantum dot random laser based on all-solution processes showed great potential for practical applications.[38] The unique advantages of the random laser can be well understood based on its underlying mechanism.[33,34] When light is emitted from a random medium, it will experience multiple scattering due to the inherent randomness of the material structure, and it can be amplified by stimulated emission. Because of the multiple scattering, there exists a threshold when the optical gain is larger than the optical loss, and the random laser occurs under this condition. Unlike conventional lasers, the rigid requirement of well-defined cavity mirrors is lifted. In our study, the emitted photons arising from the Ag-TSA MNC film play an important role as the gain medium to generate multiple scatterings to enhance the formation of closed loops. Also, from Fermi's golden rule, unlimited wave vectors, known as high-*k* modes for hyperbolic metamaterials, lead to an incremented transition rate. It is found that there is a ∼35 times enhancement in the PL of Ag-TSA MNCs when integrated with hyperbolic metamaterials in comparison with that with a silicon substrate. Quite interestingly, we also found that the random lasing action can occur at a low threshold pumping power density (∼0.5 kW cm^{-2}) at room temperature. The simulation based on the finite-difference time-domain method (FDTD) was used to confirm the observed results from experiments. Potential applications could be improved by introducing the integration of Ag-TSA MNCs with HMM, such as bioluminescence imaging, tumor imaging system, and implantable in vivo research on the human body. Therefore, the Ag-TSA MNCs with HMM provide a great advantage and open alternative ventures for researchers to take the light emission of MNCs to a high level considering the present intensive efforts in the field.

■ RESULTS AND DISCUSSION

Figure 1 and Figure S1 show the schematic diagram of the fabrication process incorporated in making the lasing device based on HMM and Ag-TSA MNCs and the device composed of Ag-TSA MNCs and silicon substrate, respectively. The silicon substrates were first cleaned in acetone, ethanol, and deionized (DI) water for 20 min to remove the absorbed contaminants. To obtain the HMM, we placed these silicon substrates inside the chamber for thermal evaporation under high vacuum conditions ($<5 \times 10^{-7}$ Torr) to deposit the gold (Au) thin film with a deposition rate of 0.3 Å/s. After that, we used raw molybdenum trioxide (MoO$_3$) powder for the deposition of the MoO$_3$ layer, keeping the deposition rate fixed at 0.3 Å/s. We repeated this procedure (Au/MoO$_3$ pair) five times to obtain the six pairs of multilayer structures, as shown in step 1 of Figure 1. To avoid the quenching effect from the emission, we deposited MoO$_3$ as the topmost layer, which served as a capping layer on the multilayers. The Ag-TSA MNCs were dropped and spin-coated onto the HMM over a silicon wafer, as shown in step 2 of Figure 1. These were further vacuum dried for 4 h at room temperature to obtain a thin film, as shown in step 3 of Figure 1. Step 4 in Figure 1 shows the schematic illustration of the random lasing device comprising the solid-state assembly of Ag-TSA MNCs over

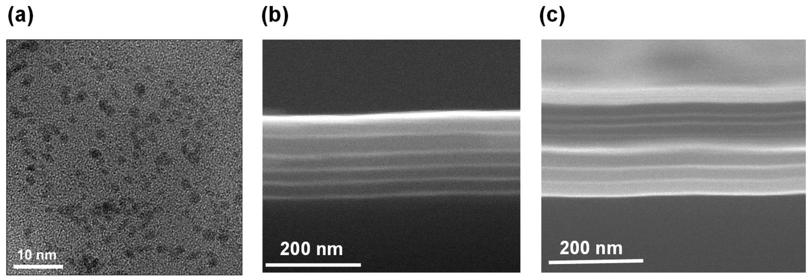

Figure 2. (a) High-resolution transmission electron microscopy (HR-TEM) image of the Ag-TSA MNCs. (b) Cross-sectional scanning electron microscopy (SEM) image of the HMM with six pairs of MoO_3/Au multilayers with a MoO_3 capping layer over the top. (c) Cross-sectional SEM image of the HMM with six pairs of MoO_3/Au multilayers with a MoO_3 capping layer over the top followed by a thin layer of Ag-TSA MNCs.

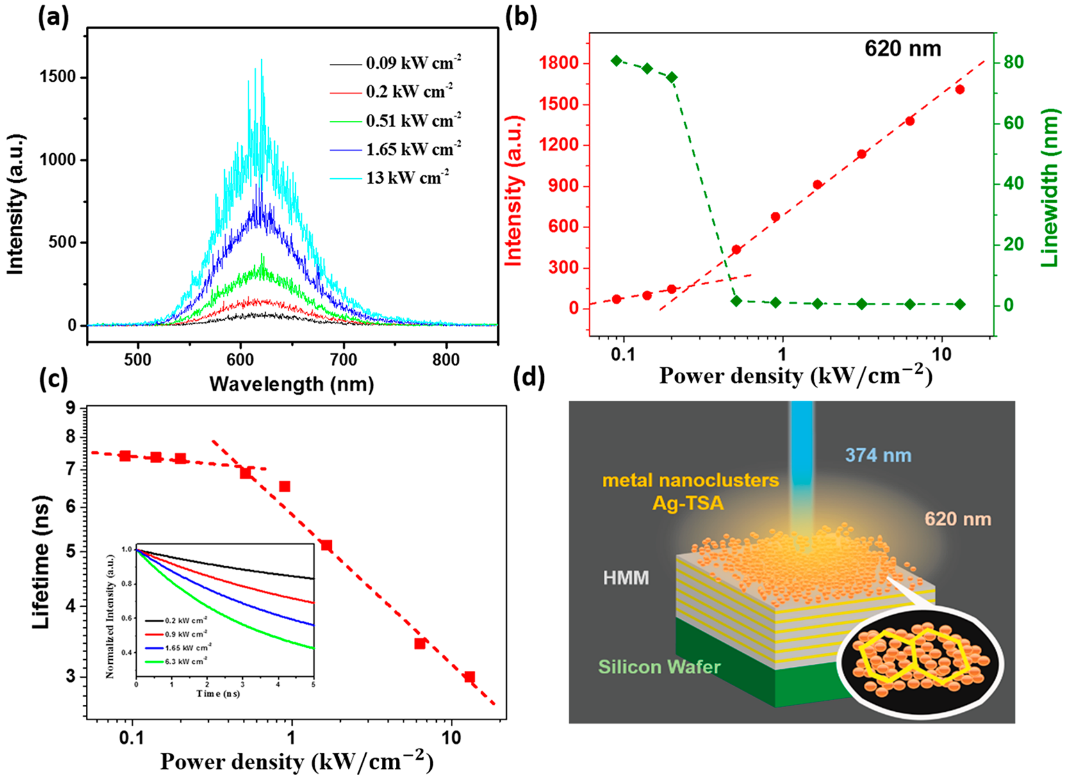

Figure 3. (a) Emission spectra of the solid-state assembly of Ag-TSA MNCs over HMM under different pumping power densities of 374 nm pulsed pump excitation. (b) Emission intensity and line width as a function of the pumping power density showcasing the low threshold value (0.5 kW cm^{-2}) of pump power density for the solid-state assembly of Ag-TSA MNCs over HMM. (c) Carrier lifetime as a function of the pumping power density for the solid-state assembly of Ag-TSA MNCs over HMM (inset: time-resolved photoluminescence (TRPL) measurements for the solid-state assembly of Ag-TSA MNCs over HMM under different pumping power densities of 374 nm pulsed pump excitation). (d) Schematic illustration of the stimulated emissions from the solid-state assembly of Ag-TSA MNCs over HMM under 374 nm pulsed pump excitation.

HMM. On the basis of the FDTD simulation, the thicknesses of Au and MoO_3 were optimized to be 7.5 and 24.5 nm, respectively. The fill fraction for Au film here was 23.43%. An 8 nm MoO_3 capping layer was deposited over HMM for the reason previously described.

MNCs were synthesized by treating Ag^+ ions with 10 mM thiosalicylic acid (TSA) under heating. The average particle size of the as-prepared Ag-TSA MNCs determined from high-resolution transmission electron microscopy (HR-TEM) measurements was 1.3 ± 0.3 nm from 50 count, as shown in Figure 2a, thus taking it into the molecular regime. When the size of the nanoclusters was comparable to the Fermi wavelength of electrons, remarkable size-dependent fluorescence properties were revealed.[33,34] Figure S2a shows the ζ potential measurements for the TSA and Ag-TSA MNCs. The surface ζ potential of Ag-TSA MNCs (−42 ± 4.7 mV) was much lower than that of free TSA in 10 mM sodium phosphate buffer (pH 7.4), ascribed to the carboxylate ions ($R\text{-}COO^-$) from TSA. The higher value of the ζ potential for the Ag-TSA MNCs confirmed the surface charge modifications due to the presence of Ag atoms. Figure S2b shows the UV−vis absorption spectra of TSA and Ag-TSA MNCs. A broad absorption band from 300 to 400 nm was attributed to TSA (Figure S2b) and ligand-to-metal charge transfers ($S \rightarrow M$) along with the possibility of ligand-to-metal−metal charge transfers ($S \rightarrow M\cdots M$) of the metal−thiolate complex on the surfaces of Ag nanocrystals.[40−43] The localized surface plasmon resonance bands due to large-sized particles were absent in the visible region, which was in good agreement with our HR-TEM analysis.[44] Furthermore, a matrix-assisted laser desorp-

https://doi.org/10.1021/acsphotonics.1c01065

tion/ionization−time-of-flight mass spectrometry (MALDI-TOF MS) measurement was carried out to identify the fine structure of the Ag-TSA MNCs through isotope pattern analysis (Figure S3). The as-prepared Ag-TSA MNC sample displayed three major *m*/*z* peaks corresponding to the $[Ag_3]$, $[Ag_3S_1]^-$, and $[Ag_2(TSA)_1\text{-}H]^-$ ions without fragmentation.[45] X-ray photoelectron spectroscopy (XPS) analysis of Ag-TSA MNCs showed distinguishable peaks centered at binding energies of 374.2 and 368.1 eV, corresponding to the characteristic peaks of Ag $3d_{3/2}$ and Ag $3d_{5/2}$, respectively (Figure S4).[46] Further deconvolution revealed the presence of a metallic core (Ag^0) and Ag^+ ascribed to the formation of a metal−thiolate complex shell. In addition, Ag-TSA MNCs clearly exhibited the S 2p peaks, indicating the dominance of the Ag_2S species and evidencing the existence of core−shell-like structures (Figure S4). The Fourier transform infrared (FT-IR) spectroscopy spectra of pristine TSA displayed peaks at 1292, 1324, 1434, 1560, 1670, and 2360 cm^{-1}, corresponding to the C−O Str., O−H bend., C−C Str., C═C Str., C═O Str., and S−H Str., respectively (Figure S5).[47] The Ag-TSA MNCs exhibited similar FT-IR bands as those of free TSA; however, a slight shift to 1298 (O−H bend), 1452 (C−C Str.), and 1689 (C = O Str.,) cm^{-1} was noticed, except for the S−H Str. band, confirming the disruption and distinctive interaction of TSA during the formation of Ag nanocrystals (Figure S5).

Figure 2b shows the cross-sectional field-emission scanning electron microscopy (FE-SEM) image of HMM with clear and flat thin films of Au and MoO_3 film. Furthermore, we coated a thin layer of Ag-TSA MNCs over the top of the HMM. The thickness of the Ag-TSA MNCs over the HMM was observed to be ∼40 nm, as shown in Figure 2c. The clear flat boundaries of the Au films generated the existence of high-*k* modes in the HMM, thus avoiding the possibility of localized resonance from the Au clusters.[48] To understand the effect of HMM on enhancing the luminescence of the Ag-TSA MNCs, we fabricated a control device with Ag-TSA MNCs coated over a silicon wafer. Figure S6a shows the schematic diagram of the experimental setup for micro-PL measurements from the solid-state assembly of Ag-TSA MNCs over a silicon wafer, where the pumping source was a 374 nm pulsed laser and the emitted wavelength from MNCs was 620 nm. Figure S6b shows the photographic image of the experimental setup. The thickness of Ag-TSA MNCs on the silicon wafer was observed to be ∼40 nm, as shown in Figure S7. The scale of the thickness of Ag-TSA MNCs on the silicon wafer (Figure S7) was fixed to what we set in the simulation from the device's cross-sectional SEM image in Figure 2c.

The PL spectra of Ag-TSA MNCs over HMM and silicon wafer are shown in Figure 3a and Figure S9a, respectively, under a 374 nm pulsed laser with different pumping power densities. The intensity increased with the pumping power density for the Ag-TSA MNCs on both the silicon wafer (Figure S8a,b) and the HMM substrate (Figure 3a,b) in the PL spectra. Comparing the PL spectra for the substrate of silicon (Figure S9a) and the HMM (Figure S9b), there is a ∼35 times enhancement in the PL intensity of Ag-TSA MNCs when integrated with HMM. Owing to the addition factor of high-*k* modes from the allowed high photonic density of states (PDOS) of the HMM, the PL can be enhanced by the underside of the HMM substrate. A sudden increase in the emission intensity was observed at a threshold pumping power density of 0.5 kW cm^{-2} only for Ag-TSA on the HMM substrate (Figure 3a) compared with that of Ag-TSA MNCs on the Si substrate (Figure S9a). Note that once a pumping power density above the threshold was applied to the device, as shown in Figure 3a, many sharp spikes appeared with a drastically increased emission intensity. Additionally, the full width at half-maximum (fwhm) of the sharp spikes dramatically decreased and dropped to <1 nm when excited by a pumping power density above the threshold, as shown in Figure 3b. The threshold behaviors of the emission intensity and the fwhm and the appearance of many sharp spikes provided clear evidence of the occurrence of random laser action.[33−37] Because the emitted photons were confined inside the Ag-TSA MNCs' random matrix, they experienced multiple scatterings. The lasing action was achieved when the incident light formed multiple closed-loop paths, which amplified the intensity of the emitted photons during scatterings. Moreover, the transition rate according to Fermi's golden rule increased due to the additional effect from the high-*k* modes in the HMM. The emitted light could propagate through the HMM to reduce the optical loss, thereby increasing the possibility of forming closed loops. Under this situation, the population inversion was achieved with a pumping power density of >0.5 kW cm^{-2}, resulting in faster transitions and thus brighter emissions. The existence of many coherent closed loops lead to the spatial profile of the random laser with a variety of sharp peaks, which was quite different from that of the conventional lasers. The temporal coherence length (L) of the laser action was calculated to be 223 μm using the formula $L = c/(n\Delta f)$, where c, n, and Δf are the velocity of light under vacuum, the refractive index of the medium, and the frequency bandwidth, respectively.[36] For a more detailed analysis of the random lasing, the power Fourier transformation (PFT) of the spectrum was performed to calculate the effective cavity length, as shown in Figure S10. The spatial dimensions could be obtained from the formula of the Fourier component, $P_m = mnL_c/\pi$, where m is the order of the Fourier harmonic, n is the gain medium refraction index (1.34), and L_c is the cavity length.[49−52] According to the relation of the Fourier peaks and the statistical distribution of the cavity length (inset of Figure S10), the effective optical cavity length was calculated to be 18.86 μm. This revealed that there exist 2D close-loop resonance paths by comparing the cavity length and the thickness of the device.

To further confirm the occurrence of laser action, we show the carrier lifetime as a function of the pumping power density for solid-state assembly of Ag-TSA MNCs over HMM in Figure 3c. The inset of Figure 3c shows the time-resolved photoluminescence (TRPL) measurements for the solid-state assembly of Ag-TSA MNCs over HMM under different pumping power densities of 374 nm pulsed pump excitation. Notably, a sublinear change of the carrier lifetime as a function of the pumping power density above the threshold value was observed. It is consistent with the observed change in emission density, which provided firm evidence of the lasing action for the solid-state assembly of Ag-TSA MNCs over HMM. To provide a better understanding of the random laser action, Figure 3d shows the schematic illustration of the stimulated emissions from the solid-state assembly of Ag-TSA MNCs over HMM under 374 nm pulsed pumped excitation. On the basis of our study, because Ag-TSA MNCs possess outstanding stimulated luminescence properties (emission of ∼620 nm, band gap of ∼2 eV) with higher quantum yields, they should

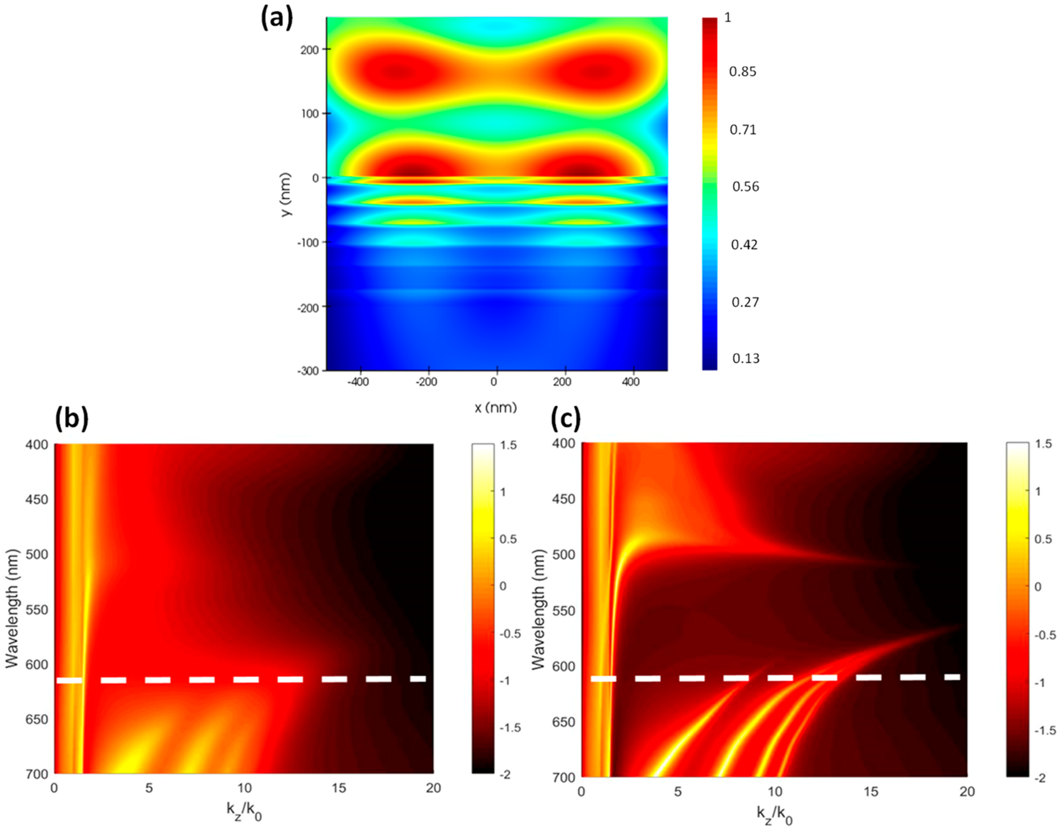

Figure 4. (a) Calculation of the electric-field intensity distributions for 620 nm emission from the solid-state assembly of Ag-TSA MNCs over HMM. (b) *k*-Space dissipated power density for the HMM (without considering the loss effect). (c) Corresponding dissipated power densities considering the loss effect. The dashed white line is the emission center of Ag-TSA metal nanoclusters at a wavelength of 620 nm.

be very useful for finding their applications in bioimaging, chemical sensing, and so on.[17,39,53]

To have a further understanding of the enhanced laser action played by the role of HMM, we performed the simulation derived from the FDTD method. Figure S11 shows the model for the solid-state assembly of Ag-TSA MNCs over HMM, where the HMM was composed of six pairs of MoO_3/Au multilayers with MoO_3 as a capping layer on the top. Figure 4a shows the electric-field profile inside the multilayer layers when a plane wave source was injected on the top of the silver MNC over the HMM and the maximum was normalized. The net charge was calculated within the monitor surface using Gauss's law by integrating the electric-field flux through the cross-sectional surface. According to electric-field distribution, it showed that a strong electric field was around the interface. In addition, the electric field could propagate in the HMM with volume plasmon polaritons to the far-field through Ag-TSA MNCs. Because of the multiple scattering of the emitted photons in the Ag-TSA MNCs matrix, the formation of coherent closed loops resulted in random lasing action. Figure 4b shows the *k*-space dissipated power density without considering the loss effect for the HMM to prove the influence of the Purcell effect. Furthermore, Figure 4c shows the corresponding dissipated power densities considering the loss effect. It shows that the strong inherent plasmonic modes can exist inside the multilayer structures at a wavelength of 620 nm. These plasmonic modes are beneficial for forming random laser action, owing to the pronounced Purcell effect. Thus the structure can be considered as a suitable composition to enhance the laser action due to the Purcell effect.

To allow the scattering process of Ag-TSA MNCs influenced by HMM substrate to stand out, we calculated the efficiency $\left(\frac{\sigma_{\text{scat}}}{A_{\text{scat}}}\right)$, as shown in Figure 5a, where σ_{scat} and A_{scat} are the scattering cross-section and the geometric cross-section, respectively. The total-field scattered-field (TFSF) source injected a plane wave from the top with an electric polarization and a wave vector to calculate the scattering efficiency. To avoid the propagation back from the simulation boundary to interact with the HMM structure again, the boundary conditions were set as perfectly matched layers. Here our proposed design of multilayer components, which combined the Ag-TSA clusters and the HMM substrates, could achieve the enhancement with a significant ratio due to the effective interaction. At a wavelength of 620 nm, the scattering efficiency showed an apparent magnitude stronger than those in the general wavelength region. It was beneficial to form the closed feedback loops due to this strong scattering effect from the interaction between the HMM substrate and the Ag-TSA MNCs. HMMs have been shown to boost the transition rates for both the spontaneous and the stimulated emission according to light−matter interactions.[54−56] In addition, stimulated emission comes along with a reduced lasing threshold due to the increased transition rate of the optical gain media. Therefore, the transition rate enhancement was followed by strong scattering efficiency that drove the lasing spectrum to be more prominent and reduced the lasing threshold to be suitable for the generation of the highly efficient random laser.

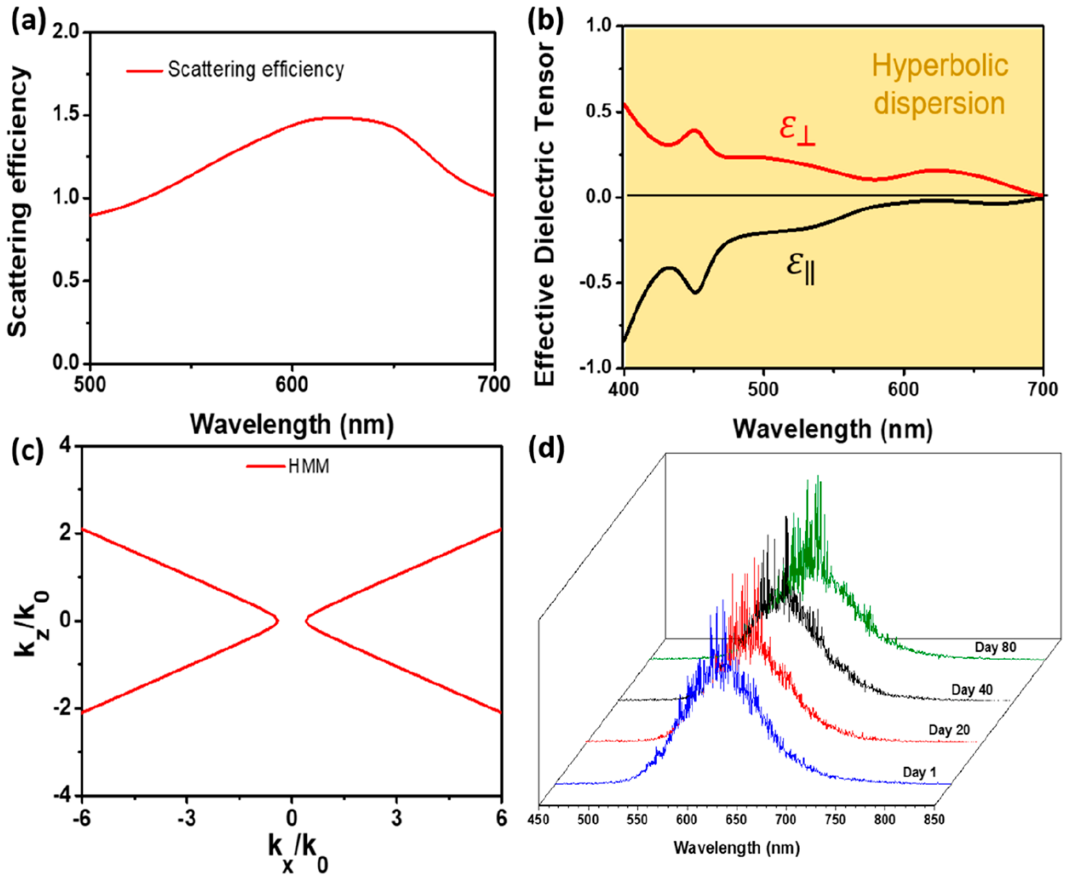

Figure 5. (a) Calculated scattering efficiency of the solid-state assembly of Ag-TSA MNCs over HMM with the highest scattering efficiency at ∼620 nm. (b) Effective dielectric tensor calculation of the HMM. All wavelengths from 400 to 700 nm are the hyperbolic dispersion ($\varepsilon_\perp \cdot \varepsilon_\parallel < 0$) in the visible spectrum. (c) Iso-frequency curve of HMM at a 620 nm emission wavelength. (d) Emission spectra from the solid-state assembly of Ag-TSA MNCs over HMM after different time durations at pumping power density of 13 kW cm^{-2}.

To verify the hyperbolic dispersion of multilayered structures, we investigated the effective dielectric tensors of the HMM. The effective permittivity tensors were considered to be homogeneous and were attributed to the effective medium theory (EMT) because the thicknesses of Au and MoO$_3$ films are much smaller than the operating wavelength. On the basis of the EMT, the dielectric tensors perpendicular ($\varepsilon_\perp$) and parallel ($\varepsilon_\parallel$) to the surface were calculated to understand the dispersion behaviors of the proposed multilayered structures with the corresponding wavelength of 620 nm, as shown in Figure 5b. All wavelengths from 400 to 700 nm were the hyperbolic dispersion ($\varepsilon_\perp \cdot \varepsilon_\parallel < 0$) in the visible spectrum. To provide evidence of the existence of high-*k* modes from the proposed HMM, the iso-frequency curve of the HMM was discussed, as shown in Figure 5c. The formula of the iso-frequency curve can be written as $\frac{k_{\perp,\mathrm{HMM}}^2}{k_0^2}\frac{1}{\varepsilon_{zz}} + \frac{k_{z,\mathrm{HMM}}^2}{k_0^2}\frac{1}{\varepsilon_{yy}} = 1$, where $k_0 = \omega/c$, the effective wave vector perpendicular ($k_{\perp,\mathrm{HMM}}$) and parallel ($k_{z,\mathrm{HMM}}$) to the optical axis of the HMM. It shows the iso-frequency curve of HMM at the 620 nm emission wavelength, which confirms the out-coupling effect of the high-*k* modes.

Finally, Figure S12 shows the angle-dependent measurement of the Ag-TSA deposited on the HMM substrate. The emission detected angle is defined as the angle between the bottom of the device and the top surface of the stage. When the device is horizontally placed without stage, it corresponds to a 0° detected angle. We can clearly see that the emission spectrum still exhibited many sharp spikes with a negligible change. It provides an addition signature for the occurrence of the random laser because one of the important characteristics of the random laser action is being angle-free. Figure 5d presents the stability of the device under different time intervals with a fixed pumping energy density of 13 kW cm^{-2}. The results presented a very pronounced random laser action showing high stability that made it suitable for numerous applications ranging from biomedical to chemical sensing and optoelectronic applications.

■ CONCLUSIONS

We have made an attempt to demonstrate the integration of HMM with Ag-TSA MNCs to achieve low-threshold random lasing actions and enhanced stimulated emissions. A proper alternate multilayer design of metal and dielectric layers is used to fabricate an HMM substrate suitable for achieving lasing actions. When placed on a silicon substrate, Ag-TSA MNCs exhibit only spontaneous emissions, whereas Ag-TSA MNCs, when integrated with an HMM substrate, enable enhanced stimulated emissions to be emitted. The emission intensity is enhanced ∼35 times for Ag-TSA MNCs with HMM in comparison with Ag-TSA MNCs on a silicon substrate. The low threshold value so obtained to achieve lasing action is ∼0.5 kW cm^{-2} under 374 nm pulsed pumped excitations. The rough interface between the solid-state assembly of Ag-TSA MNCs and the HMM assists in the propagation of the out-coupling

https://doi.org/10.1021/acsphotonics.1c01065

power of the high-*k* modes to the far field, thereby not letting the emitted light get trapped inside the layered structure. This is beneficial for enhanced random lasing action at low thresholds. The experimental results are well supported by the FDTD simulations. The presence of high-*k* modes in the HMM provides strong proof for enhanced stimulated emissions. We believe that our study based on the integration of Ag-TSA MNCs and HMM enables us to broaden the application of optoelectronic devices covering solid-state lighting to bioimaging and so on. Additionally, our approach only serves as an initial step to trigger many other alternatives to generate laser action out of MNCs, which is very useful for the development of more advanced applications.

■ EXPERIMENTAL METHODS

Materials. Sinapinic acid (SA) and silver nitrate ($AgNO_3$) were purchased from Sigma-Aldrich (St. Louis, MO). TSA, sodium phosphate monobasic monohydrate ($NaH_2PO_4\cdot H_2O$), sodium phosphate dibasic heptahydrate ($Na_2HPO_4\cdot 7H_2O$), and ethyl alcohol (EtOH) were obtained from Acros Organics (Geel, Belgium). Acetonitrile (ACN) was procured from Alps Chemicals (Gujrat, India). Milli-Q ultrapure water (18.2 MΩ cm) from Millipore (Billerica, MA) was used in the experimental analysis.

Synthesis of Ag-TSA MNCs. To prepare the Ag-TSA MNCs, we added $AgNO_3$ (5 mM) to the vial containing TSA (10 mM) dispersed in 1.0 mL of DI water. Then, the solution was heated to 70 °C for 1 h to obtain bright yellow precipitates. The resulting solution was cooled to room temperature and subjected to centrifugation at a relative centrifugal force (RCF) of 5000*g* at 4 °C for 20 min and washed three time with EtOH (≥99.5% v/v). The purified Ag-TSA MNC solution was stored at 4 °C for further experimental analysis.[57,58]

Characterization of Ag-TSA MNCs. UV−vis absorption spectra of Ag-TSA MNCs were measured using a double-beam UV−vis spectrophotometer (Cintra 10e, GBC, Victoria, Australia). The PL spectra of Ag-TSA MNCs were recorded at an excitation wavelength of 330 using a Cary Eclipse Varian spectrofluorometer (Walnut Creek, CA). The HR-TEM analysis of Ag-TSA MNCs was performed using field-emission transmission electron microscopy (FE-TEM) equipped with a dual focused ion beam (FIB) system. The mass spectra of Ag-TSA MNCs were recorded in a linear positive-ion mode using an Autoflex Speed MALDI-TOF mass spectrometer (Bruker Daltonics, Bremen, Germany). The Ag-TSA MNCs (5.0 μL) were homogenized with 5.0 μL of SA matrix solution (10 mg mL^{-1} of SA in 5:5:0.01 (v/v/v) ACN/water/trifluoroacetic acid), from which 1.0 μL of mixture was dropped onto a stainless-steel 384-well MALDI plate and vacuum-dried at room temperature for 12 h before the MALDI-MS analysis. A nitrogen laser (10 Hz, 337 nm) was used to irradiate the crystallized Ag-TSA MNCs. Desorbed ions were stabilized during a delayed extraction period of 800 ns and were then again accelerated through the TOF chamber prior to entering the mass analyzer. The accelerating voltage was fixed at +20 kV. The binding energy of Ag-TSA MNCs was recorded using XPS measurements by a VG ESCA210 apparatus from VG Scientific (West Sussex, U.K.). All of the binding energies were corrected using C 1s (284.6 eV) as an internal standard. 100 μL of Ag-TSA MNCs was coated onto the Si substrate and vacuum-dried at room temperature prior to the XPS analysis. FT-IR spectra of Ag-TSA MNCs were obtained using a Nicolet iS5 FT-IR spectrometer (Thermo Scientific, Waltham, MA).

Fabrication of HMM Multilayer Structure. A silicon wafer was used to design the multilayer structure. The silicon substrates were first cleaned in acetone, ethanol, and DI water for 20 min to remove the absorbed contaminants. To obtain HMM, we placed these silicon substrates inside the chamber for thermal evaporation under high vacuum conditions ($<5 \times 10^{-7}$ Torr) to deposit the gold (Au) thin film with a deposition rate at 0.3 Å/s. Thereafter, we used raw MoO_3 powder for the deposition of the MoO_3 layer, keeping the deposition rates fixed at 0.3 Å/s. We repeated this procedure (Au/MoO_3 pair) five times to get the six pairs of multilayer structures. To avoid the quenching effect from the emission, we deposited MoO_3 as the topmost layer , which served as a capping layer on the multilayers. The Ag-TSA MNCs were dropped and spin-coated onto the HMM over the silicon wafer. These were further vacuum dried for 4 h at room temperature to obtain a thin film of Ag-TSA MNCs. The ultrapure raw materials including gold (Au) and MoO_3 were purchased from Sigma-Aldrich.

Optical and Microscopy Measurements. The PL measurements were performed under a 374 nm pulsed diode laser (Picoquant, PDL 800-B, center wavelength 374 nm, 70 ps, 2.5 MHz). The PL spectra were recorded using a Horiba Jobin Yvon TRIAX 320 spectrometer. A time-corrected single-photon counting (Pico Harp 300) system was used for time-resolved PL measurements with a time resolution of ∼36 ps from the function of instrument response. The FE-SEM images were recorded on a JEOL JSM-6500F apparatus. All of the characterizations of the device were performed under ambient conditions.

Numerical Simulations. The commercial electromagnetic software Lumerical was used to obtain the results of the simulations shown in this work. The electric-field polarization for the incident wave was set along the x direction, which was launched from the top of the simulation region. The refractive indices of Au and MoO_3 were obtained from Bohren et al.[59] The refractive index for the Ag-TSA MNCs was set from Shabaninezhad et al.[60] To avoid unwanted artificial numerical results from the borderline of the computational (simulation) region, we used a perfectly matched layer in all simulation directions, which resulted in an infinitesimal spatial space. The mesh setup was set at 2 nm to obtain highly accurate calculated results.

■ ASSOCIATED CONTENT

Supporting Information

The Supporting Information is available free of charge at https://pubs.acs.org/doi/10.1021/acsphotonics.1c01065.

> Schematic diagram of the fabrication process followed in fabricating the device composed of Ag-TSA MNCs and silicon substrate. Zeta potential of free TSA and Ag-TSA. UV−vis absorption of TSA and Ag-TSA MNCs. MALDI-TOF mass spectra of TSA-Ag nanocrystals. XPS spectra for TSA-Ag nanocrystals. FT-IR spectroscopy spectra of TSA and Ag-TSA MNCs. Schematic diagram to show the experimental setup of Micro-PL measurements from the solid-state assembly of Ag-TSA MNCs. Photographic image of the experimental setup. Cross-sectional SEM image of Ag-TSA MNCs over silicon wafer. Emission spectra and emission intensity as

a function of pumping power density spectra of the solid-state assembly of Ag-TSA MNCs over silicon. A comparison of the emission spectra state assembly of Ag-TSA over silicon and HMM substrate. PFT intensity–frequency relation graph. Theoretical model for the solid-state assembly of Ag-TSA MNCs over HMM. Emission spectra of Ag-TSA over HMM substrate with different sample holder angles (PDF)

AUTHOR INFORMATION

Corresponding Author

Yang-Fang Chen – *Department of Physics, National Taiwan University, Taipei 106, Taiwan; Advanced Research Centre for Green Materials Science and Technology, National Taiwan University, Taipei 10617, Taiwan;* orcid.org/0000-0003-1203-5115; Email: yfchen@phys.ntu.edu.tw

Authors

Chao-Chu Wang – *Department of Physics, National Taiwan University, Taipei 106, Taiwan;* orcid.org/0000-0002-3866-3702

Monika Kataria – *Department of Physics, National Taiwan University, Taipei 106, Taiwan; Institute of Atomic and Molecular Sciences, Academia Sinica, Taipei 115, Taiwan;* orcid.org/0000-0003-4912-340X

Hung-I Lin – *Department of Physics, National Taiwan University, Taipei 106, Taiwan;* orcid.org/0000-0001-9849-3138

Amit Nain – *Department of Chemistry, National Taiwan University, Taipei 106, Taiwan; Nanoscience and Nanotechnology Program, Taiwan International Graduate Program, Institute of Physics, Academia Sinica, Taipei 106, Taiwan; Department of Engineering and System Science, National Tsing Hua University, Hsinchu 300, Taiwan*

Hsia Yu Lin – *Department of Physics, National Taiwan University, Taipei 106, Taiwan;* orcid.org/0000-0002-0886-3367

Christy Roshini Paul Inbaraj – *Department of Physics, National Taiwan University, Taipei 106, Taiwan;* orcid.org/0000-0002-8776-9917

Yu-Ming Liao – *Department of Physics, National Taiwan University, Taipei 106, Taiwan;* orcid.org/0000-0002-8696-7313

Anjali Thakran – *Department of Physics, National Taiwan University, Taipei 106, Taiwan;* orcid.org/0000-0003-1250-2166

Huan-Tsung Chang – *Department of Chemistry, National Taiwan University, Taipei 106, Taiwan; Department of Chemistry, Chung Yuan Christian University, Taoyuan City 32023, Taiwan;* orcid.org/0000-0002-5393-1410

Fan-Gang Tseng – *Department of Engineering and System Science and Frontier Research Center on Fundamental and Applied Sciences of Matters, National Tsing Hua University, Hsinchu 300, Taiwan; Division of Mechanics, Research Center for Applied Sciences, Academia Sinica, Taipei 115, Taiwan;* orcid.org/0000-0001-7654-6905

Ya-Ping Hsieh – *Institute of Atomic and Molecular Sciences, Academia Sinica, Taipei 115, Taiwan;* orcid.org/0000-0002-6065-751X

Complete contact information is available at: https://pubs.acs.org/10.1021/acsphotonics.1c01065

Author Contributions

¶C.-C.W., M.K., and H.-I.L. contributed equally. Y–F.C. and M.K. planned and supervised the overall project. M.K. and C.-C.W. designed the experiments, fabricated the device, and performed optical measurements. A.N. synthesized the Ag-TSA MNCs and performed the characterization measurements. C-C.W. and H.-I.L. performed the theoretical simulations. H.Y.L. contributed to the FE-SEM images. M.K., C.R.P.I., Y.-M.L., A.T., H.-T.C., F.-G.T., Y.-P.H., and Y.-F.C. discussed the mechanism of metal nanoclusters and hyperbolic metamaterials. All of the authors contributed to writing the manuscript.

Notes

The authors declare no competing financial interest.

ACKNOWLEDGMENTS

This work was financially supported by the "Advanced Research Centre for Green Materials Science and Technology" from The Featured Area Research Centre Program within the framework of the Higher Education Sprout Project by the Ministry of Education (108L9006) and the Ministry of Science and Technology in Taiwan (MOST 108-3017-F-002-002, MOST 108-2112-M-002-019).

REFERENCES

(1) Zare, I.; Chevrier, D. M.; Cifuentes-Rius, A.; Moradi, N.; Xianyu, Y.; Ghosh, S.; Trapiella-Alfonso, L.; Tian, Y.; Shourangiz-Haghighi, A.; Mukherjee, S.; et al. Protein-protected Metal Nanoclusters as Diagnostic and Therapeutic Platforms for Biomedical Applications. *Mater. Today* **2021**, DOI: 10.1016/j.mattod.2020.10.027.

(2) Yuan, P.; Zhang, R.; Selenius, E.; Ruan, P.; Yao, Y.; Zhou, Y.; Malola, S.; Häkkinen, H.; Teo, B. K.; Cao, Y.; et al. Solvent-mediated Assembly of Atom-precise Gold–silver Nanoclusters to Semiconducting One-dimensional Materials. *Nat. Commun.* **2020**, *11*, 1–8.

(3) Lv, M.; Zhou, W.; Fan, D.; Guo, Y.; Zhu, X.; Ren, J.; Wang, E. Illuminating Diverse Concomitant DNA Logic Gates and Concatenated Circuits with Hairpin DNA-Templated Silver Nanoclusters as Universal Dual-Output Generators. *Adv. Mater.* **2020**, *32*, 1908480.

(4) Shah, P.; Nagda, R.; Jung, I. L.; Bhang, Y. J.; Jeon, S.-W.; Lee, C. S.; Do, C.; Nam, K.; Kim, Y. M.; Park, S.; et al. Noncanonical Head-to-Head Hairpin DNA Dimerization is Essential for the synthesis of Orange Emissive Silver Nanoclusters. *ACS Nano* **2020**, *14*, 8697–8706.

(5) Mu, J.; Yang, J.-L.; Zhang, D.-W.; Jia, Q. Progress in Preparation of Metal Nanoclusters and Their Application in Detection of Environmental Pollutants. *Chin. J. Anal. Chem.* **2021**, *49*, 319–329.

(6) Galchenko, M.; Black, A.; Heymann, L.; Klinke, C. Field Effect and Photoconduction in Au_{25} Nanoclusters Films. *Adv. Mater.* **2019**, *31*, 1900684.

(7) Maity, S.; Bain, D.; Patra, A. An overview on the current understanding of the photophysical properties of metal nanoclusters and their potential applications. *Nanoscale* **2019**, *11*, 22685–22723.

(8) Grassian, V. H. When Size Really Matters: Size-Dependent Properties and Surface Chemistry of Metal and Metal Oxide Nanoparticles in Gas and Liquid Phase Environments. *J. Phys. Chem. C* **2008**, *112*, 18303–18313.

(9) Kelly, K. L.; Coronado, E.; Zhao, L. L.; Schatz, G. C. The Optical Properties of Metal Nanoparticles: the Influence of Size, Shape, and Dielectric Environment. *J. Phys. Chem. B* **2003**, *107*, 668–677.

(10) Yau, S. H.; Varnavski, O.; Goodson, T. An Ultrafast Look at Au Nanoclusters. *Acc. Chem. Res.* **2013**, *46*, 1506–1516.

(11) Jin, R.; Zeng, C.; Zhou, M.; Chen, Y. Atomically Precise Colloidal Metal Nanoclusters and Nanoparticles: Fundamentals and Opportunities. *Chem. Rev.* **2016**, *116*, 10346–10413.

(12) Du, X.; Jin, R. Atomic-precision Engineering of Metal Nanoclusters. *Dalton Trans.* **2020**, *49*, 10701−10707.

(13) Garzón, I. L.; Reyes-Nava, J. A.; Rodriguez-Hernandez, J. I.; Sigal, I.; Beltrán, M.; Michaelian, K. Chirality in Bare and Passivated Gold Nanoclusters. *Phys. Rev. B: Condens. Matter Mater. Phys.* **2002**, *66*, No. 073403.

(14) Kang, X.; Zhu, M. Tailoring the Photoluminescence of Atomically Precise Nanoclusters. *Chem. Soc. Rev.* **2019**, *48* (2422), 2457.

(15) Goswami, N.; Yao, Q.; Luo, Z.; Li, J.; Chen, T.; Xie, J. Luminescent Metal Nanoclusters with Aggregation-induced Emission. *J. Phys. Chem. Lett.* **2016**, *7*, 962−975.

(16) Guo, Y.; Zhao, X.; Long, T.; Lin, M.; Liu, Z.; Huang, C. Histidine-mediated Synthesis of Chiral Fluorescence Gold Nanoclusters: Insight into the Origin of Nanoscale Chirality. *RSC Adv.* **2015**, *5*, 61449−61454.

(17) Yang, J.; Jin, R. Advances in Enhancing Luminescence of Atomically Precise Ag Nanoclusters. *J. Phys. Chem. C* **2021**, *125*, 2619−2625.

(18) Valizadeh, A.; Mikaeili, H.; Samiei, M.; Farkhani, S. M.; Zarghami, N.; Kouhi, M.; Akbarzadeh, A.; Davaran, S. Quantum Dots: Synthesis, Bioapplications, and Toxicity. *Nanoscale Res. Lett.* **2012**, *7*, 1−14.

(19) Ma, J.; Chen, J.-Y.; Zhang, Y.; Wang, P.-N.; Guo, J.; Yang, W.-L.; Wang, C.-C. Photochemical Instability of Thiol-capped CdTe Quantum Dots in Aqueous Solution and Living Cells: Process and Mechanism. *J. Phys. Chem. B* **2007**, *111*, 12012−12016.

(20) Matus, M. F.; Häkkinen, H. Atomically Precise Gold Nanoclusters: Towards an Optimal Biocompatible System from a Theoretical-Experimental Strategy. *Small* **2021**, *17*, 2005499.

(21) Rival, J. V.; Mymoona, P.; Lakshmi, K. M.; Nonappa; Pradeep, T.; Shibu, E. S. Self-Assembly of Precision Noble Metal Nanoclusters: Hierarchical Structural Complexity, Colloidal Superstructures, and Applications. *Small* **2021**, *17*, 2005718.

(22) Deng, H.-H.; Shi, X.-Q.; Wang, F.-F.; Peng, H.-P.; Liu, A.-L.; Xia, X.-H.; Chen, W. Fabrication of Water-soluble, Green-emitting gold nanoclusters with a 65% Photoluminescence Quantum Yield *via* Host−guest Recognition. *Chem. Mater.* **2017**, *29*, 1362−1369.

(23) Soldan, G.; Aljuhani, M. A.; Bootharaju, M. S.; AbdulHalim, L. G.; Parida, M. R.; Emwas, A.-H.; Mohammed, O. F.; Bakr, O. M. Gold Doping of Silver Nanoclusters: a 26-Fold Enhancement in the Luminescence Quantum Yield. *Angew. Chem., Int. Ed.* **2016**, *55*, 5749−5753.

(24) Poddubny, A.; Iorsh, I.; Belov, P.; Kivshar, Y. Hyperbolic Metamaterials. *Nat. Photonics* **2013**, *7*, 948−957.

(25) Huang, J.; Zhang, D.; Wang, H. Epitaxial TiN/MgO Multilayers with Ultrathin TiN and MgO layers as Hyperbolic Metamaterials in Visible Region. *Mater. Today Phys.* **2021**, *16*, 100316.

(26) Lin, H.-I.; Shen, K.-C.; Liao, Y.-M.; Li, Y.-H.; Perumal, P.; Haider, G.; Cheng, B. H.; Liao, W.-C.; Lin, S.-Y.; Lin, W.-J.; et al. Integration of Nanoscale Light Emitters and Hyperbolic Metamaterials: An Efficient Platform for the Enhancement of Random Laser Action. *ACS Photonics* **2018**, *5*, 718−727.

(27) Redding, B.; Choma, M. A.; Cao, H. Speckle-free laser imaging using random laser illumination. *Nat. Photonics* **2012**, *6*, 355−359.

(28) Shen, K. C.; Ku, C. T.; Hsieh, C.; Kuo, H. C.; Cheng, Y. J.; Tsai, D. P. Deep-Ultraviolet Hyperbolic Metacavity Laser. *Adv. Mater.* **2018**, *30*, 1706918.

(29) Zhang, L.; Yu, W.; Wang, Q.; Ou, J.-Y.; Wang, B.; Tang, G.; Jia, X.; Yang, X.; Wang; Cai, G. X. Electronic and hyperbolic dielectric properties of ZrS2/HfS2 heterostructures. *Phys. Rev. B: Condens. Matter Mater. Phys.* **2019**, *100*, 165304.

(30) Tonkaev, P.; Anoshkin, S.; Pushkarev, A.; Malureanu, R.; Masharin, M.; Belov, P.; Lavrinenko, A.; Makarov, S. Acceleration of radiative recombination in quasi-2D perovskite films on hyperbolic metamaterials. *Appl. Phys. Lett.* **2021**, *118*, No. 091104.

(31) Shafi, M.; Liu, R.; Zha, Z.; Li, C.; Du, X.; Wali, S.; Jiang, S.; Man, B.; Liu, M. Highly efficient SERS substrates with different Ag interparticle nanogaps based on hyperbolic metamaterials. *Appl. Surf. Sci.* **2021**, *555*, 149729.

(32) Chandrasekar, R.; Wang, Z.; Meng, X.; Azzam, S. I.; Shalaginov, M. Y.; Lagutchev, A.; Kim, Y. L.; Wei, A.; Kildishev, A. V.; Boltasseva, A.; et al. Lasing Action with Gold Nanorod Hyperbolic Metamaterials. *ACS Photonics* **2017**, *4*, 674−680.

(33) Cao, H.; Zhao, Y. G.; Ho, S. T.; Seelig, E. W.; Wang, Q. H.; Chang, R. P. H. Random Laser Action in Semiconductor Powder. *Phys. Rev. Lett.* **1999**, *82*, 2278−2281.

(34) Wiersma, D. The Physics and Applications of Random Lasers. *Nat. Phys.* **2008**, *4*, 359−367.

(35) Kataria, M.; Yadav, K.; Nain, A.; Lin, H.-I.; Hu, H.-W.; Paul Inbaraj, C. R.; Chang, T.-J.; Liao, Y.-M.; Cheng, H.-Y.; Lin, K.-H.; et al. Self-sufficient and Highly Efficient Gold Sandwich Upconversion Nanocomposite Lasers for Stretchable and Bio-applications. *ACS Appl. Mater. Interfaces* **2020**, *12*, 19840−19854.

(36) Haider, G.; Lin, H.-I.; Yadav, K.; Shen, K.-C.; Liao, Y.-M.; Hu, H.-W.; Roy, P. K.; Bera, K. P.; Lin, K.-H.; Lee, H.-M.; et al. A Highly-Efficient Single Segment White Random Laser. *ACS Nano* **2018**, *12*, 11847−11859.

(37) Hsu, Y.-T.; Tai, C.-T.; Wu, H.-M.; Hou, C.-F.; Liao, Y.-M.; Liao, W.-C.; Haider, G.; Hsiao, Y.-C.; Lee, C.-W.; Chang, S.-W.; et al. Self-Healing Nanophotonics: Robust and Soft Random Lasers. *ACS Nano* **2019**, *13*, 8977−8985.

(38) Shen, T. L.; Hu, H. W.; Lin, W. J.; Liao, Y. M.; Chen, T. P.; Liao, Y. K.; Lin, T. Y.; Chen, Y. F. Coherent Förster Resonance Energy Transfer: A New Paradigm for Electrically Driven Quantum Dot Random Lasers. *Sci. Adv.* **2020**, *6*, eaba1705.

(39) Desireddy, A.; Conn, B. E.; Guo, J.; Yoon, B.; Barnett, R. N.; Monahan, B. M.; Kirschbaum, K.; Griffith, W. P.; Whetten, R. L.; Landman, U. Ultrastable Silver Nanoparticles. *Nature* **2013**, *501*, 399−402.

(40) Kawawaki, T.; Ebina, A.; Hosokawa, Y.; Ozaki, S.; Suzuki, D.; Hossain, S.; Negishi, Y. Thiolate-Protected Metal Nanoclusters: Recent Development in Synthesis, Understanding of Reaction, and Application in Energy and Environmental Field. *Small* **2021**, *17*, 2005328.

(41) Chen, Y.; Yang, T.; Pan, H.; Yuan, Y.; Chen, L.; Liu, M.; Zhang, K.; Zhang, S.; Wu, P.; Xu, J. Photoemission Mechanism of Water-soluble Silver Nanoclusters: Ligand-to-metal−metal Charge Transfer *vs* Strong Coupling between Surface Plasmon and Emitters. *J. Am. Chem. Soc.* **2014**, *136*, 1686−1689.

(42) Wu, Z.; Jin, R. On the Ligand's Role in the Fluorescence of Gold Nanoclusters. *Nano Lett.* **2010**, *10*, 2568−2573.

(43) Goswami, N.; Yao, Q.; Chen, T.; Xie, J. Mechanistic Exploration and Controlled Synthesis of Precise Thiolate-gold Nanoclusters. *Coord. Chem. Rev.* **2016**, *329*, 1−15.

(44) Hutter, E.; Fendler, J. H. Exploitation of Localized Surface Plasmon Resonance. *Adv. Mater.* **2004**, *16*, 1685−1706.

(45) Rao, T. U. B.; Nataraju, B.; Pradeep, T. Ag9 Quantum Cluster through a Solid-state Route. *J. Am. Chem. Soc.* **2010**, *132*, 16304−16307.

(46) Le Guével, X.; Hötzer, B.; Jung, G.; Hollemeyer, K.; Trouillet, V.; Schneider, M. Formation of Fluorescent Metal (Au, Ag) Nanoclusters Capped in Bovine Serum Albumin Followed by Fluorescence and Spectroscopy. *J. Phys. Chem. C* **2011**, *115*, 10955−10963.

(47) Tan, Y.; Wang, Y.; Jiang, L.; Zhu, D. Thiosalicylic Acid-functionalized Silver Nanoparticles Synthesized in One-phase System. *J. Colloid Interface Sci.* **2002**, *249*, 336−345.

(48) Andryieuski, A.; Zhukovsky, S. V.; Lavrinenko, A. V. Rough Metal and Dielectric Layers Make an Even Better Hyperbolic Metamaterial Absorber. *Opt. Express* **2014**, *22*, 14975−14980.

(49) Polson, R. C.; Vardeny, Z. V. Random Lasing in Human Tissues. *Appl. Phys. Lett.* **2004**, *85*, 1289−1291.

(50) Hu, Z.; Zhang, Q.; Miao, B.; Fu, Q.; Zou, G.; Chen, Y.; Luo, Yi.; Zhang, D.; Wang, P.; Ming, H.; Zhang, Q. Coherent Random Fiber Laser Based on Nanoparticles Scattering in the Extremely Weakly Scattering Regime. *Phys. Rev. Lett.* **2012**, *109*, 253901.

(51) Bian, Y.; Shi, X.; Hu, M.; Wang, Z. A Ring-Shaped Random Laser in Momentum Space. *Nanoscale* **2020**, *12*, 3166−3173.

(52) Wu, M.-J.; Wu, S.-C.; Shen, T.-L.; Liao, Y.-M.; Chen, Y.-F. Anderson Localization Enabled Spectrally Stable Deep-Ultraviolet Laser Based on Metallic Nanoparticle Decorated AlGaN Multiple Quantum Wells. *ACS Nano* **2021**, *15*, 330−337.

(53) Udaya Bhaskara Rao, T.; Pradeep, T. Luminescent Ag7 and Ag8 Clusters by Interfacial Synthesis. *Angew. Chem., Int. Ed.* **2010**, *49*, 3925−3929.

(54) Shen, K.-C.; Hsieh, C.; Cheng, Y.-J.; Tsai, D. P. Giant enhancement of emission efficiency and light directivity by using hyperbolic metacavity on deep-ultraviolet algan emitter. *Nano Energy* **2018**, *45*, 353−358.

(55) Yang, X.; Yao, J.; Rho, J.; Yin, X.; Zhang, X. Experimental realization of three-dimensional indefinite cavities at the nanoscale with anomalous scaling laws. *Nat. Photonics* **2012**, *6*, 450−454.

(56) Cortes, C. L.; Newman, W.; Molesky, S.; Jacob, Z. Quantum nanophotonics using hyperbolic metamaterials. *J. Opt.* **2012**, *14*, No. 063001.

(57) Nain, A.; Tseng, Y.-T.; Lin, Y.-S.; Wei, S.-C.; Mandal, R. P.; Unnikrishnan, B.; Huang, C.-C.; Tseng, F.-G.; Chang, H.-T. Tuning the photoluminescence of metal nanoclusters for selective detection of multiple heavy metal ions. *Sens. Actuators, B* **2020**, *321*, 128539.

(58) Pan, S.; Liu, W.; Tang, J.; Yang, Y.; Feng, H.; Qian, Z.; Zhou, J. Hydrophobicity-Guided Self-Assembled Particles of Silver Nanoclusters with Aggregation-Induced Emission and Their Use in Sensing and Bioimaging. *J. Mater. Chem. B* **2018**, *6*, 3927−3933.

(59) Bohren, C. F.; Huffman, D. R. *Absorption and Scattering of Light by Small Particles* **1998**, 1−530.

(60) Shabaninezhad, M.; Ramakrishna, G. Theoretical Investigation of Plasmonic Properties of Quantum-Sized Silver Nanoparticles. *Plasmonics* **2020**, *15*, 783−795.

https://doi.org/10.1021/acsphotonics.1c01065